Catalysis Letters
https://doi.org/10.1007/s10562-021-03609-5

CO_2 Hydrogenation over Ru-NPs Supported Amine-Functionalized SBA-15 Catalyst: Structure–Reactivity Relationship Study

Vivek Srivastava[1]

Received: 19 January 2021 / Accepted: 18 March 2021

Abstract

We gave an effective protocol to support Ru NPs on amine-functionalized SBA-15 mesoporous silica to catalyze the CO_2 hydrogenation reaction. The amine groups present in the catalytic system performed an essential role in stabilizing the Ru NPs, delivering the robust metal-support interaction and improved catalytic activities to material in formic acid synthesis. We also demonstrated a comprehensive study of different amine groups on the catalytic performance of ultrafine uniformly dispersed Ru NPs over mesoporous SBA-15 support. The effect of various compositional and steric properties of amine groups on the size/distribution of the Ru NPs were closely studied and correlated with their catalytic performance in the CO_2 hydrogenation reaction. The in situ DRIFTS analysis of CO_2 hydrogenation into formic acid in presence of developed CATALYST-1 showed active surface species bonded to support sites and to Ru NPs. This interaction proposed the formation of important intermediates such as hydrides, formates and bicarbonates, which are significant for the formation of formic acid. We successfully recycled the catalysts up to 5 runs with good catalytic activity.

Graphic Abstract

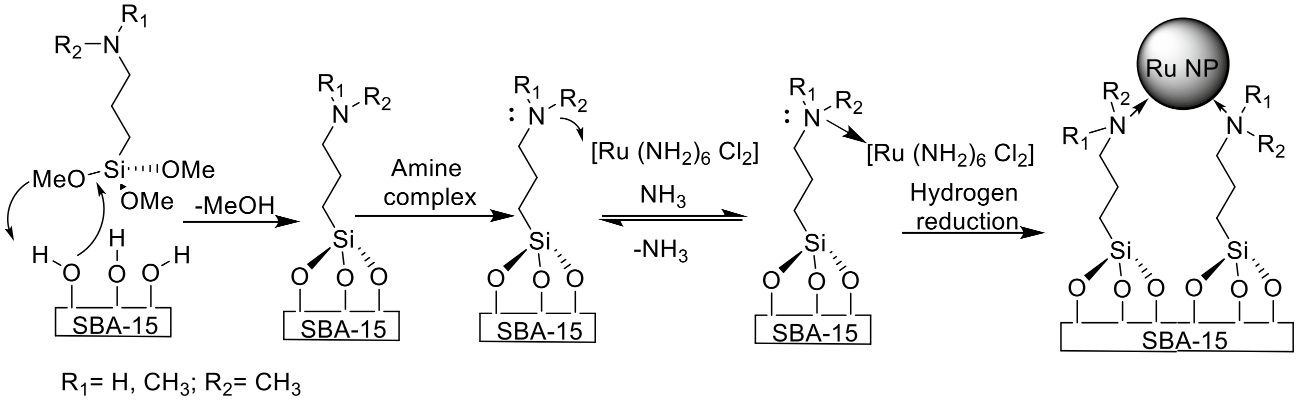

Keywords SBA-15 · Formic acid · Carbon sequestration · Hexaammineruthenium (III) complexes · Amine-functionalized silica

1 Introduction

Carbon dioxide gas is one of the important products of the combustion process and is not counted as a benign molecule of the atmosphere. The quantity of CO_2 in the atmosphere has touched extraordinary levels and remains to rise owing to a rising rate of fossil fuel burning, triggering apprehension

---

✉ Vivek Srivastava
vivek.shrivastava@niituniversity.in

[1] Mathematics & Basic Sciences, NIIT University, NH-8 Jaipur/Delhi Highway, Neemrana, Rajasthan 301705, India

about climate change, and increasing sea levels [1]. Considering the above, a conceivable solution to this problem is the utilization of carbon dioxide. Scholars in this area are using different approaches to convert CO_2 gas into useful chemicals. However, this creates the challenge of employing a large volume of seized CO_2, which earlier has not had any industrially practical uses at such a large scale [2]. Realizing that, historically, fossil reserves were created via natural carbon-hydrogenation during photosynthesis, synthetic CO_2 hydrogenation is likely the best way to regenerate combusted hydrocarbons [3, 4].

While CO_2 hydrogenation is difficult due to the high thermal stability of CO_2 molecules, substantial development has been made for transforming CO_2 to single carbon (C1) products such as formic acid, methane, and methanol using direct hydrogen reduction [5–7].

Formic acid has gained much consideration due to its several applications as raw material/intermediate, in food technology, agriculture, leather, and rubber industries [8]. Furthermore, formic acid is considered as one of the encouraging hydrogen storage materials, which has a volumetric hydrogen density of 53 g/L of H_2 and is suitable to store and transport in the liquid state under ambient conditions [9, 10]. As per the literature reviews, different techniques for the synthesis of formic acid from CO_2 have been established, such as photocatalytic reduction, electrochemical processes, enzymatic conversion, and hydrogenation [11–16]. The above procedures comprise of two steps: (1) carbonylation of methanol to methyl format ($HCOOCH_3$) and (2) hydrolysis of $HCOOCH_3$ to HCOOH [11, 12, 16]. Unfortunately, the above method also suffers due to the use of toxic CO for methanol carbonylation. Also, the formic acid can be made from CO_2 using the following reactions such as hydrogenation, carbonation, and hydration [5, 7, 10–12].

Various homogeneous metal complexes have been widely explored as a catalyst for CO_2 hydrogenation to formic acid, but they normally suffer from the difficulty to isolate and reuse of the catalyst [17–21]. Although some hybrid heterogenized homogeneous catalysts have been reported to address the demerits of the homogeneous such as post-immobilizing homogenous metal complexes on inorganic or organic supports such as silica and polymers [9, 18, 22]. Unfortunately, the above approach repeatedly ends with low activity and selectivity due to changes in the chemical and electronic structure of the metal catalytic centers. Moreover, the requirement of costly ligands also hinders its large-scale application in CO_2 hydrogenation.

Heterogeneous catalysts showed noticeable improvements in easy product separation and catalyst recycling [23]. Various Au, Pt, Ru, Ir, Cu, etc. metals were supported on different inorganic supports such as MMT clay, Silica, TiO_2, etc. to catalyze CO_2 hydrogenation to format or formic acid [24–27]. It was also noticed that in some of the reports catalyst support were also found as an important factor to promote the reaction kinetics of CO_2 hydrogenation reaction due to the presence of surface functional groups with supports, such as the presence of Schiff base on the Au/SiO_2-Schiff catalyst [28] and nitrogen functionalities on the Pd/C_3N_4 catalyst [29]. However, the described heterogeneous catalysts still suffer from some demerits such as restricted chemical designability, low reactivity comparing with homogeneous ones, comparatively low product concentration, and requirement of toxic polar organic solvents [30]. Therefore, it is necessary to create a cost-effective heterogeneous catalytic system for CO_2 hydrogenation to format or formic acid. In line with this, wide efforts have been engrossed in the reaction protocol to improve the reactivity by increasing the density of supported metal, reducing the size of metal particles, and regulating the morphologies as well as surface characteristics of support [23, 31–33]. As a result, competent heterogeneous catalysts were typically designed by immobilizing metal nanoparticles (NPs) on a variety of supports such as ionic liquid, polymers, MMT clay, metal oxides, TiO_2, graphene, and silica, etc. [17, 27, 29–36]. However, the stacked metal NPs in catalysts are suitable to aggregate thus leading to a decrease in their catalytic capacity. This is principally attributing to their large surface-to-volume ratio and higher surface free energy in contrast with their bulk equivalents [23, 33]. To defeat the challenges mentioned above and enhance the catalytic activity as well as stability, metal NPs-based catalysts were prepared by embedding the NPs on the inner surface of the interlayer of the support.

In this report, we have developed a series of amine-functionalized nonporous silica materials to anchor Ru NPs. We also studied the relationship among different types of amine functionality, Ru NPs, and the catalytic property of the developed material for CO_2 hydrogenation reaction. We also demonstrated and designed amine-functionalized SBA-15 supported Ru NPs where we used all three types of amines such as primary, secondary, and tertiary. After performing the comprehensive analysis of all the developed amine-functionalized SBA-15 supported Ru NPs, their catalytic performance was tested for CO_2 hydrogenation reaction and correlated the effect of amines, size of Ru NPS, physiochemical properties of support in terms of formic acid quantity.

2 Experimental

All the chemicals were purchased from Sigma Aldrich and other chemical suppliers. Elemental analysis was carried out with Perkin Elmer Optima 3300 XL ICP-OES. Standard Bruker 300WB Nuclear Magnetic Resonance (NMR) spectrometer with an Avance console at 400 and 100 MHz was used to record ^{1}H NMR. The morphology of catalysts was investigated by transmission electron microscopy (TEM) using a Philips CM12 instrument. Kratos-Axis 165 with Mg Kα radiation 1254 eV was used to perform X-ray photoelectron spectroscopy (XPS). DTA-TGA thermal analyzer apparatus (Shimadzu DTG-60H) was used to study the thermal stability of all the developed materials. BET surface area, pore size, and pore volume measurements of the catalysts were determined from physical adsorption of N_2 using liquid nitrogen by an ASAP2420 Micromeritics adsorption analyzer (Micromeritics Instruments Inc). The surface area and pore size distribution were calculated using BET and BJH equations by the instrument software. All the hydrogenation reactions were performed in a 100-mL stainless steel autoclave (Amar Equipment, India). UV–Vis diffuse reflectance spectroscopy was carried out with a Cary 5000 UV–Vis spectrometer (Agilent).

2.1 Synthesis of SBA-15 Silica

The SBA-15 was synthesized using Pluronic ® P123 as a templating agent in acidic solution as per the reported literature [37]. In a simple experimental procedure, the reaction vessel was charged with Pluronic ® P123, 10 M HCl, tetraethyl orthosilicate (TEOS), and deionized water with the molar mass ratio of 1:7:2:18. The combined reaction was vigorously stirred at 50 °C for 24 h. Then the resulting solution was aged at 70 °C for the next 24 h. After cooling the reaction mass, a solid mass was recovered by washing with deionized water (5 × 2 mL). The unutilized Pluronic ® P123 templet was isolated from the resulting white solid by dispersing the same in the mixture of ethanol and diethyl ether (1:1 ratio). The slurry was stirred for 5 h at 50 °C. Then the resulting white solid material was washed with diethyl (5 × 2 ml) ether and ethanol (7 × 2 mL). Later, the perfectly washed materials were dried at 40 °C in a vacuum oven and the final material was named ET-SBA-15.

2.2 Synthesis of Amine-Functionalized SBA-15 Silica Using Three Different Types of Amine

The reaction vessel was charged with ET-SBA-15 (1 g), dry toluene (70 mL) and (3-Aminopropyl) trimethoxysilane (APTMS) or *N*-Methylaminopropyltrimethoxysilane (MAPTMS) or 3-(*N*,*N*-dimethylamino propyl) trimethoxysilane (DMAPTMS) (1.4 mmol). The combined reaction mass was vigorously stirred for 5 h at 75 °C. After colling the reaction mass, the resulting solid mass was washed with toluene (5 × 2 mL) and then ethanol (5 × 2 mL). The perfectly washed solid materials were dried in a vacuum oven at 40 °C. The resulting white powder was named SBA-15 -PAN (primary amine, $-NH_2$) SBA-15-SAN (secondary amine, $-NHCH_3$), and SBA-15- TAN (tertiary amine, $-N(CH_3)_2$).

2.3 Synthesis of Hexaammineruthenium (III) Chloride and Derivatives [38]

The reaction vessel was charged with $RuCl_3.3H_2O$ (0.7 g), water (5 mL), and hydrazine hydrate (5 mL, 85% solution). The combined reaction was refluxed for 2 h, then after cooling the reaction mass was filtered by gravity. Easy reaction workup was performed using ammonium chloride solution. The canary-yellow color precipitate was collected by simple filtration and the same was washed with a small quantity of ice-cold aqueous ammonia solution (3 × 2 mL), ethanol (3 × 2 mL), and in last with ether (3 × 2 mL). The resulting materials were dried at 40 °C under vacuum for 2 h (0.40 g, 60% yield). Please note the material radially decomposes on exposure to air. $[Ru\ (NH_3)_6\ Cl_3]$ Anal. Calcd. For $H_{18}Cl_3N_6Ru$: N, 27.13; H, 5.81; Cl^-, 34.41. Found N, 27.04; H, 5.80; Cl^-, 34.1.

Two hexaammineruthenium (III) complexes were synthesis, by mixing $RuCl_3.3H_2O$ (0.65 g) with three different types of amines such as methylamine (1.8 gm) or dimethylamine (1.91 g) in presence of hydrazine hydrate (5 mL, 85% solution). The above reaction mass was refluxed for 2 h, then after cooling the same, it was washed with a small quantity of ice-cold aqueous ammonia solution (3 × 2 mL), ethanol (3 × 2 mL), and last with ether (3 × 2 mL). The resulting materials $[Ru\ (NH_3)_6\ Cl_3]$ was dried at 40 °C under vacuum for 2 h (0.40 g, 60% yield). Please note the material radially decomposes on exposure to air.

$[Ru\ (NH_2\ CH_3)_6\ Cl_3]$ Anal. Calcd. For $C_6H_{30}Cl_2N_6Ru$: C, 18.30; H, 7.68; Cl, 27.01; N, 21.34; Ru, 25.67 Found C, 18.20; H, 7.47; Cl, 27.21; N, 21.30; Ru, 25.78.

$[Ru\ (NH\ (CH_3)_2)_6\ Cl_3]$ Anal. Calcd. For $C_{12}H_{42}Cl_2N_6Ru$: C, 30.16; H, 8.86; Cl, 22.25; N, 17.58; Ru, 21.15 Found C, 30.01; H, 8.76; Cl, 22.30; N, 17.41; Ru, 21.10.

2.4 Synthesis of Ru Complex Ion Anchored Amine-Functionalized SBA-15 Mesoporous Silica Materials

The reaction flask was charged with $[Ru\ (NH_2)_6Cl_3]$ (0.5 g), ethanol (2 mL), deionized water (5 mL) and amine-functionalized SBA-15 (1 g) such as SBA-15 -PAN (primary amine, $-NH_2$) SBA-15-SAN (secondary amine, $-NHCH_3$) and SBA-15-TAN (tertiary amine, $-N(CH_3)_2$). The mixture was stirred for 5 h at 80 °C. Then solid material was filtered through centrifugation (at 2000 rpm for 5 min) and washed with water (5 × 2 mL). The perfectly washed material was dried under vacuum at 40 °C. We obtained the desired product SBA-15-PAN@Ru (III), SBA-15-SAN@Ru (III), and SBA-15-TAN@Ru (III) in good quantity.

The controlled sample ET-SBA-15 @Ru (III) was also prepared as per the above protocol by mixing ET-SBA-15 with $[Ru\ (NH_2)_6Cl_3]$.

2.5 Synthesis of Ru (0) Anchored Amine-Functionalized SBA-15 Mesoporous Silica Materials

The SBA-15-PAN@Ru (III), SBA-15-SAN@Ru (III), and SBA-15-TAN@Ru (III) and ET-SBA-15- @Ru (III) materials were reduced by using 15% of H_2/N_2 at 250 °C for 2 h to convert Ru (III) ions into the Ru (0) NPs. The representative materials isolated were named as SBA-15-PAN@Ru (0), SBA-15-SAN@Ru (0), and SBA-15-TAN@Ru (0) and ET-SBA-15@Ru (0) (control material).

2.6 CO_2 Hydrogenation Reaction and Formic Acid and Catalyst Recycling

All the catalytic reactions were carried out in a 50 mL stainless steel autoclave equipped with a magnetic stirrer. In a simple experimental procedure, the reactor was charged with catalyst, water, and other reactants as per Table 3, entry 1–19. Then after closing the reactor, the air in the reactor was replaced with CO_2 and the reactor was kept at 60 °C for 30 min. Then the reactor was pressurized with H_2 gas to get the desired pressure. After charging all the required reactants, the reaction mass was stirred for the appropriate time and temperature as per Table 3. After completion of the reaction, the reaction mass was allowed to cool. Later the catalyst was isolated by centrifugation method. Then using nitrogen gas at ambient pressure, formic acid was distilled at 130 °C.

The recovered catalyst was washed with ether to remove the organic impurity from the surface of the catalyst. Then, the catalyst was pretreated at 45 °C for 10 min under 10 MPa pressure of hydrogen gas. After the pretreatment of the catalyst, all the reaction steps were repeated as per the above procedure to obtain the recycling result.

3 Result and Discussion

3.1 Preparation and Physicochemical Analysis of Amine-Functionalized SBA-15 Mesoporous Silica

We developed a series of SBA-15 mesoporous silica materials using three different types of amines (primary amine (PAN), secondary (SAN), and tertiary (TAN)) as per the

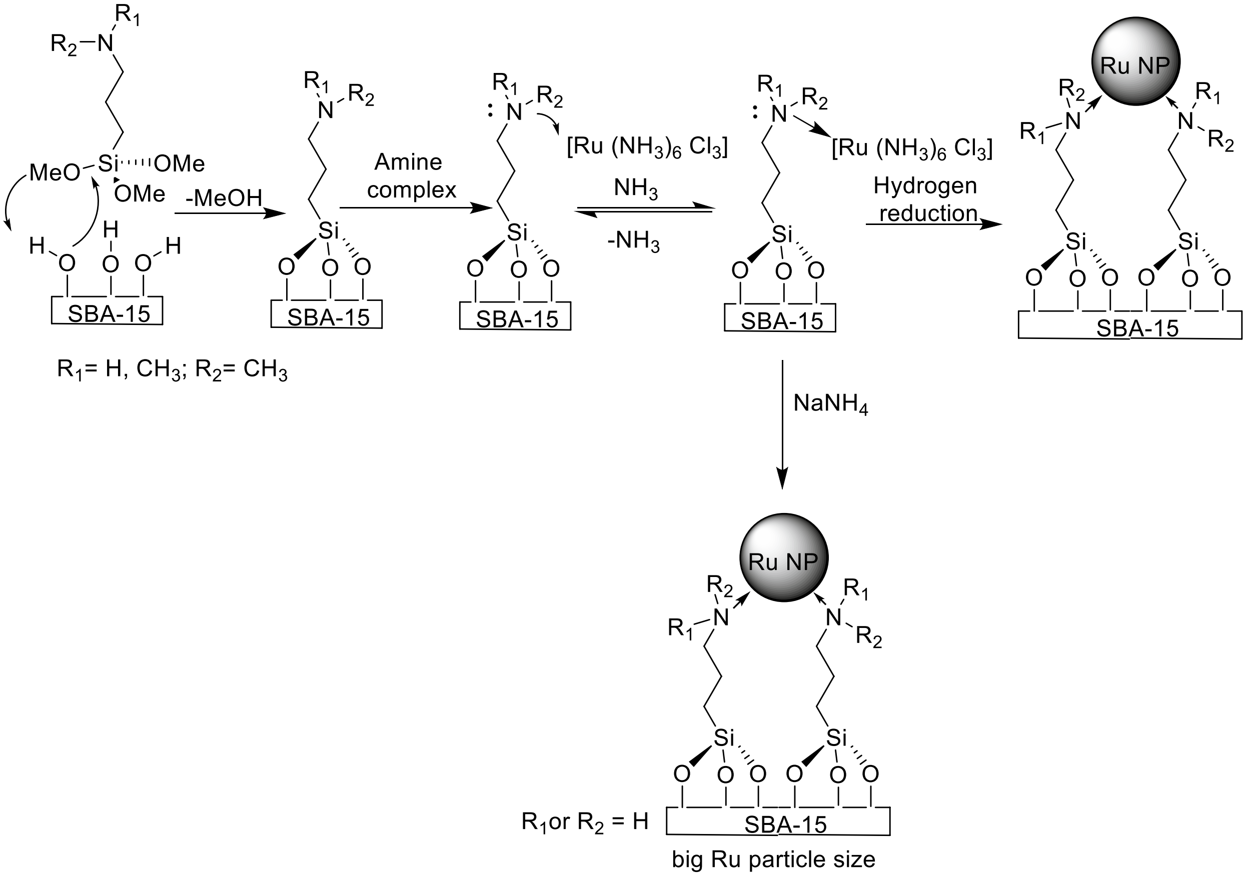

Scheme 1 Synthetic procedure for different SBA-15 materials with and without Ru metal

reported procedure with slight modification (scheme 1) [39]. The surface Si–OH groups of surfactant-extracted SBA-15 mesoporous silica (ET-SBA-15) were anchored with three types of 3-aminoaloxysilanes such as (3-Aminopropyl) trimethoxysilane (APTMS), *N*-Methylaminopropyltrimethoxysilane (MAPTMS), and 3-(*N*,*N*-dimethylaminopropyl) trimethoxysilane (DMAPTMS).

The ET-SBA-15 was developed by eliminating the Pluronic ® P123 templets from the as -formulated mesoporous silica using a solvent extraction method [37, 40, 41]. Even if it does not get free of the templates, this technique "*as countered to calcination*" was preferred for eliminating the templates here, because it leaves behind the significantly desired (in our case), higher density of Si–OH groups. A better density of Si–OH functional groups is favorable in our case because it allows the grafting of a higher density of organoamine functional group onto the SBA-15 material. Here, the above functional groups can be utilized as co-catalysts in CO_2 reduction reaction and formic acid synthesis. Additionally, the large density organoamine functional groups are helpful to upload the higher density of Ru (III) ions over SBA-15 materials. Moreover, a substantial amount of the outstanding Pluronic ® P123 templates comes out from ET-SBA-15 material during the following steps: subsequent grafting step at 80 °C for 5 h, the solvent extraction process, and reduction step at 250 °C for 2 h (when Ru NPS formed) (Scheme 1). TGA analysis of Pluronic ® P123 showed the thermal degradation of the material at 250 °C. This data confirms that we can obtain the Pluronic ® P123 impurity-free material at this temperature. Hence, the catalytic activity of the material does not compromise due to the presence of residual templates as an impurity. While performing the grafting process of aminoorganoaloxysilane, the Si–OH functional groups in ET-SBA-15 material work as nucleophiles. As a result, they create organoamine functional groups that are covalently linked to the surface of ET-SBA-15 followed by Si–O-Si bonds. In this process, the formation of the methanol molecule was noticed as a by-product (Scheme 1). As per the above protocol, three different types of amine groups (PAN, SAN, and TAN) were attached to the surface of ET-SBA-15 by using their corresponding alkoxysilane precursors and gave three types of amine-functionalized SBA-15 such as SBA-15 -PAN, SBA-15-SAN, and SBA-15-TAN respectively as per scheme 1.

Table 1 Physiochemical analysis of different SBA-15 materials

Material	N[a] (mmol/g_{cat})	BET[b] surface area (m^2/g)	Pore size[c] (nm)	Pore volume[c] (cm^3/g)
ET-SBA-15	N/A	348	6.2	0.49
SBA-15-PAN	2.7	278	4.8	0.21
SBA-15-SAN	2.6	231	4.1	0.17
SBA-15-TAN	2.9	298	3.8	0.11

[a] Calculated based on EA

[b] Calculated based on N_2 adsorption/desorption data

[c] Calculated using BJH adsorption isotherm equation

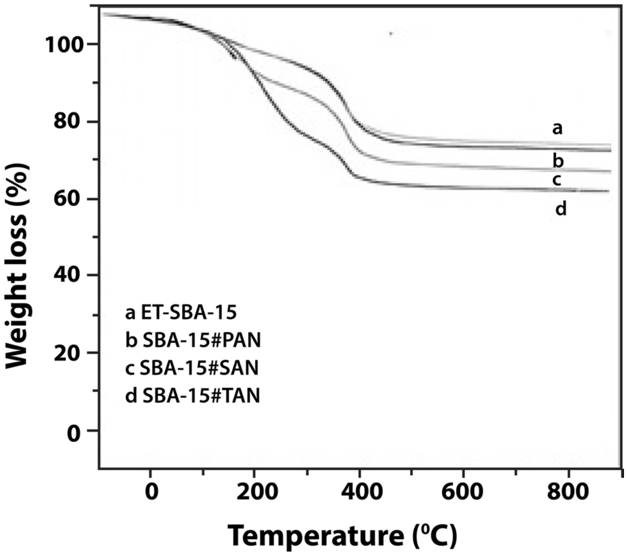

Fig. 1 TGA analysis data of neat ET-SBA-15 and other amine-functionalized SBA-15 materials

We performed a comprehensive analytical study such as elemental analysis (EA), thermogravimetric analysis (TGA), and N_2 porosimetry to characterize the physicochemical properties of all the above-synthesized materials. As per Table 1, the details of elemental analysis for all types of amine-functionalized SBA-15 (SBA-15-PAN, SBA-15-SAN, and SBA-15-TAN) were tabulated. It is worth notify that a nearly similar amount of nitrogen (2.0–2.6 mmol g_{cat}^{-1}) was recorded in all types of amine-functionalized SBA-15 materials. TGA analysis data of neat ET-SBA-15 and other amine-functionalized SBA-15 materials were displayed in Fig. 1. The 1st weight loss of 0.75% in ET-SBA-15 was recorded from room temperature to 120 °C due to the evaporation of water molecules from the ET-SBA-15 structure. A 2nd weight loss (near to 17%) was noticed from the temperature range 120–700 °C due to the loss of outstanding polymers and water followed by the condensation of Si–OH groups. While performing the TGA analysis for SBA-15-PAN, SBA-15-SAN, and SBA-15-TAN materials to distinct weight loss from room temperature to 120 °C due to evaporation of residual water from the surface of the material and then from 120–700 °C the degradation of template polymers and water (by the condensation of Si–OH groups) as well as the decomposition of organoamine group (*ca.* 12%) respectively. The above TGA analysis results confirmed the almost similar quantity of organoamine moieties in all SBA-15-PAN, SBA-15-SAN, and SBA-15-TAN materials.

In, N$_2$ adsorption/desorption measurements of amine-functionalized SBA-15 materials lower surface area was reported with respect to ET-SBA-15 material due to the pores in the SBA-15-PAN, SBA-15-SAN, and SBA-15-TAN materials were partially occupied surface organoamine groups as a result of organosilane grafting (Fig. 2a and b). Additionally, the N$_2$ gas adsorption/desorption data of all the materials shown a type IV isotherm with hysteresis loops, signifying the existence of mesoporous materials as well as also confirmed the memory effect of the mesoporous structure in the materials during organoamine functionalization. Also, due to the grafting of bulky organoamines over SBA-15 increasingly reduced the pore size of the materials. Notably, a drop in average BJH pore diameters for all the materials (ET-SBA-15, SBA-15-PAN, SBA-15-SAN, and SBA-15-TAN) was found in the range of 6.9–3.8 nm respectively (Table 1 and Fig. 2a and b). Despite the presence of heavier grafting groups, the slightly higher surface area was recorded in SBA-15-PAN, and SBA-15-SAN. This discrimination was recorded due to the functionalization of SBA-15-TAN with more nonfunctionalized groups. BET surface area analysis confirmed the effective cross-sectional area of N$_2$ on silica surface ranging between 16 Å and 21 Å (may vary with the surface modification of silica). Although several types of corrections were considered to obtain the effective cross-sectional area of N$_2$ interaction, the BET surface area analysis cannot be accurate, and it may vary with the nature of nanoporous silica material modified with non-polar functional moieties. Considering the above, the BET surface area value was higher for SBA-15-TAN than SBA-15-PAN and SBA-15-SAN.

3.2 Preparation and Physicochemical Analysis of a Series of Ru Ion Anchored Amine-Functionalized SBA-15 Mesoporous Silica Materials

The Ru ions were immobilized into amine-functionalized SBA-15 materials (SBA-15-PAN, SBA-15-SAN, and SBA-15-TAN) was achieved by reacting the solution of SBA-15 -PAN or SBA-15-SAN or SBA-15-TAN with a solution of hexaammineruthenium (III) chloride complex ([Ru (NH$_3$)$_6$] Cl$_3$). To monitor the interaction of hexaammineruthenium (III) complex with the grafted amine functional groups of ET-SBA-15 material were characterized by UV–Vis diffuse reflectance spectroscopy. We obtained the absorption maximum (λ_{max}) for all SBA-15-PAN, SBA-15-SAN, and SBA-15-TAN was recorded in the range between 280–300 nm (attributable to interbank transition in the metal-amine complex) (Fig. 3a and b). Notably, the absorption data for all the above-mentioned materials gave a red-shift compared with the control sample of amine-free SBA-15@Ru ($\lambda_{max} = 282$ nm). A clear increase in absorption maxima was recorded while increasing the number of methyl substituents in the amine group: SBA-15-PAN ($\lambda_{max} = 286$ nm), SBA-15-SAN ($\lambda_{max} = 294$ nm) and SBA-15-TAN ($\lambda_{max} = 301$ nm). Comparably, red-shift was recorded in the three control samples synthesized by mixing unmodified ET-SBA-15 with three types of hexaammineruthenium (III) chloride complexes, [Ru (NH$_3$)$_6$]Cl$_3$, [Ru (NH$_2$CH$_3$)$_6$]Cl$_{3,}$ and [Ru (NH(CH$_3$)$_2$)$_6$]Cl$_3$. As per the UV–Vis spectra of the above complexes, the redshift is often due to the following three possible reasons; a. *N*-Methylation of amine groups of metal amine complex creates an anodic shift in the redox potential; b. *N*-Methylation of amine groups generally increases the electron density due to the increase of N atom makes the amine functionality to be good σ-donor.; c. *N*-Methylation

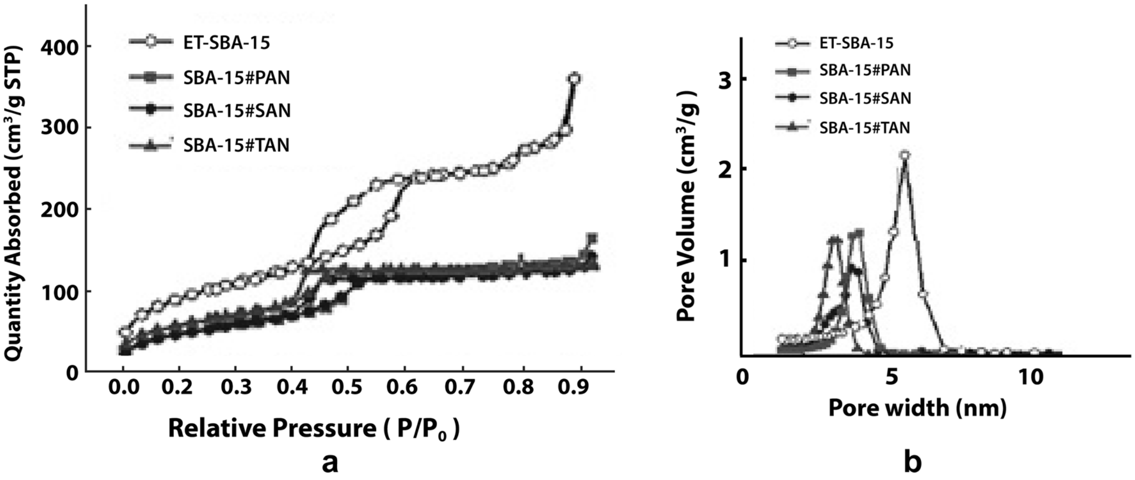

a

b

Fig. 2 **a** N$_2$ Adsorption/desorption profiles, **b** N$_2$ Adsorption/desorption profiles of SBA-15 materials

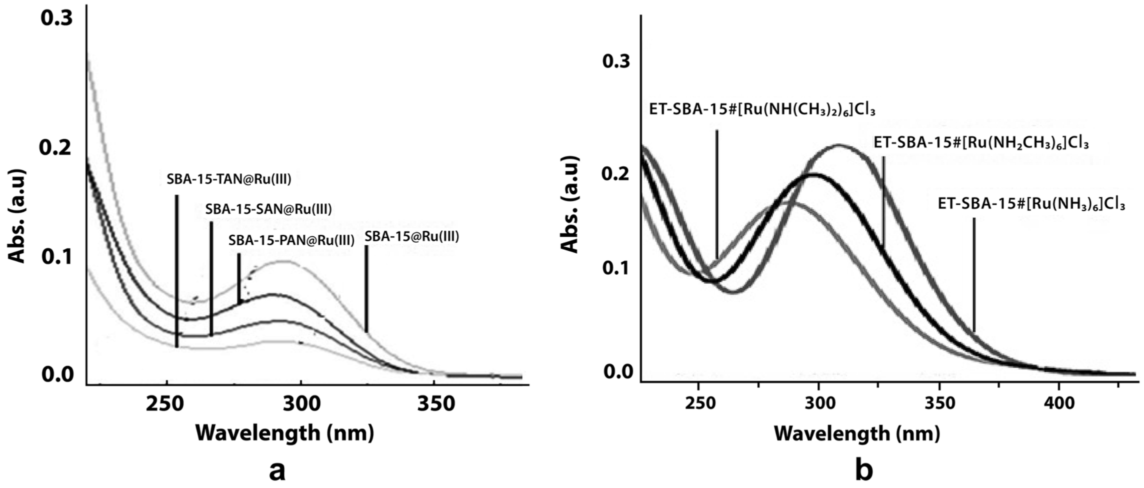

Fig. 3 **a** UV–Vis data for amine functionalized SBA-15 with Ru (II) metal, **b** UV–Vis data for amine functionalized SBA-15 with ruthenium complex species

also lowers the degree of solvation of metal- amine complex (Fig. 3a and b). As per the above reasons, in presence of polar protic solvents, tertiary amines are widely examined as poorer σ-donor and poorer ligand in compression with primary and secondary amines. Thus, because of it, the formation of Metal-Nitrogen-H- -O hydrogen bonds to the solvent molecules make the primary and secondary amines stronger σ-donors. Additionally, the steric hindrance due to the increase of methyl groups elongated the M–N bonds and distorted the coordination sphere around Ru ions in the complexes. As per the above discussion the red-shift in the charge transfer band upon more *N*-Methylation of the ligands to be due to the gradually weakening σ electron-donating nature of the nitrogen atoms of the amine ligands.

3.3 Preparation and Physicochemical Analysis of a Series of Ru (0) Anchored Amine-Functionalized SBA-15 Mesoporous Silica Materials/Catalysts

After the grafting of the organoamine groups and immobilization of Ru ions on the surface of ET-SBA-15, the corresponding material was further reduced under molecular H_2 gas at 250 °C. As a result of the above process, we obtained grayish colored powder of Ru metal immobilized-amine functionalized SBA-15 with different amine groups SBA-15-PAN@Ru (0) (CATALYST-1), SBA-15-SAN@Ru (0) (CATALYST-2), and SBA-15-TAN@Ru (0) (CATALYST-3) (Fig. 4a and b). All the synthesized materials were analyzed by EA, ICP-OES, N_2 porosimetry and the corresponding results were tabulated in Table 2. The EA and ICP-OES experimental results indicated the quantity of nitrogen was identical (1.3–1.5 mmol g_{cat}^{-1}) while the amount of Ru metal varied from 0.16–0.41 mmol g_{cat}^{-1}. Although the same molar quantity of amine-functionalized SBA-15 materials (SBA-15-PAN, SBA-15-SAN, and SBA-15-TAN) were used to react with the identical moles of Ru precursors, the final product SBA-15-PAN@Ru (0) (CATALYST-1), SBA-15-SAN@Ru (0) (CATALYST-2) and SBA-15-TAN@Ru (0) (CATALYST-3) showed the variation in the quantity of Ru metal due to the differences in the hydrophobicity of organoamines which were grafted on the materials. More precisely, as per Table 2, the Ru metal loading in catalyst 2 and catalyst 3 was lesser than catalyst 1 due to the weaker ability of hexaammineruthenium (III) ions to anchor onto SBA-15-SAN and SBA-15-TAN than SBA-15-PAN.

The N_2 adsorption/desorption data of CATALYST-1, CATALYST-2, and CATALYST-3 gave type IV isotherm with hysteresis loops. This data confirmed the original intact structure of SBA-15-PAN, SBA-15-SAN, and SBA-15-TAN materials even at comparatively high temperatures under H_2 pressure. Additionally, the BET surface areas of CATALYST-1, CATALYST-2, and CATALYST-3 were found lower than their corresponding amine-functionalized SBA-15 materials (SBA-15-PAN, SBA-15-SAN, and SBA-15-TAN) (Table 2). Moreover, these materials also showed lower average BJH pore diameters and pore volumes while increasing the bulky organoamine groups in amine-functionalized SBA-15 materials.

All the catalysts and amine-free SBA-15@Ru(0) were characterized by TGA. All the catalysts gave 0.62% of initial weight loss while elevating the temperature from room temperature to 120 °C due to residual water in the structure of the catalysts (Fig. 5). A second weight loss of 12% was recorded while increasing the temperature from 120 and 700 °C mainly because of the organoamine decomposition

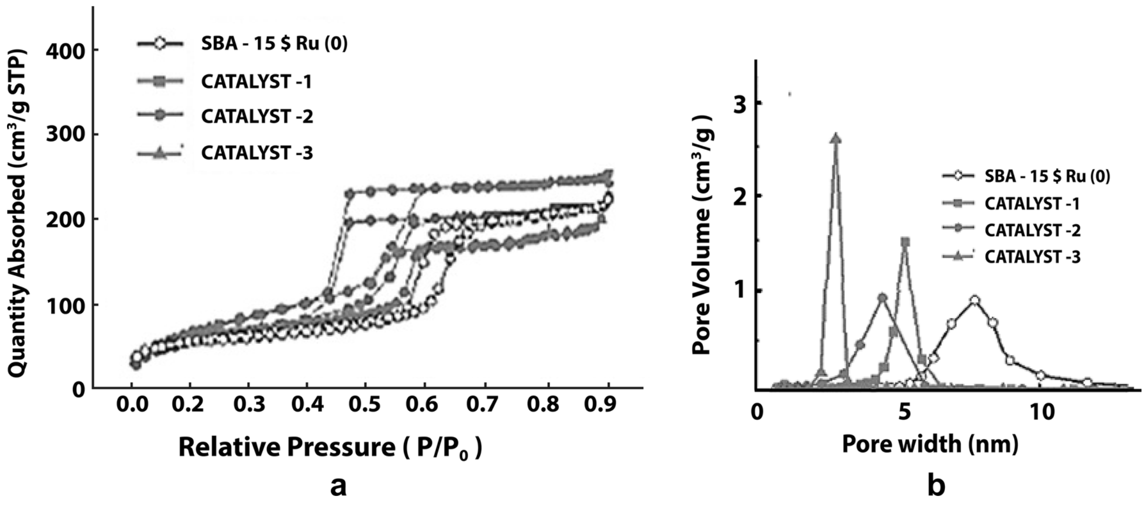

Fig. 4 **a** N_2 Adsorption/desorption profiles, **b** N_2 Adsorption/desorption profiles of different SBA-15 materials with Ru(0) NPs

and water (followed by condensation of Si–OH groups in the materials). While in the control sample of SBA-15@Ru(0) 1.3% weight loss was recorded between the temperature range between room temperature to 120 °C (due to the removal of water) and 7.6% weight loss between the temperature range from 120 to 700° (due to the removal of residual Pluronic polymer templates and water due to the condensation of Si–OH groups).

Table 2 Physiochemical analysis of different Ru anchored SBA-15 materials

Material	N^a ($mmol/g_{cat}$)	BET^b surface area (m^2/g)	Pore size^c (nm)	Pore volume^c (cm^3/g)	Ru (0)^d ($mmol/g_{cat}$)
ET-SBA-15	N/A	163	9.3	0.22	–
CATALYST -1	2.6	185	7.8	0.27	0.43
CATALYST -2	2.7	197	4.5	0.24	0.15
CATALYST -3	3.1	243	4.8	0.35	0.16

[a] Calculated based on EA

[b] Calculated based on N_2 adsorption/desorption data by BET method

[c] Calculated using BJH adsorption isotherm equation by BET method

[d] Calculated by ICP-OES analysis

To inspect the effect of different amine groups on the size and the dispersion of Ru NPS over the support in all the catalysts were analyzed by transmission electron microscopy (TEM) (Fig. 6). Narrow size and uniformly distributed Ru NPS were recorded over the SBA-15@Ru(0), CATALYST-1, CATALYST-2, and CATALYST-3 materials. However, the Ru NP size varies with respect to amine-functionalized SBA-15 materials. The smallest Ru NPs were noticed in CATALYST-1 (4.5 nm (±0.25)) and an almost identical Ru NP size was recorded in CATALYST-2 (9.6 nm (±0.25)), but in CATALYST-3 much bigger Ru NPs were found (17.9 nm (±0.25)). Biggest Ru NPs was recoded in SBA-15@Ru(0) (32.7 nm (±0.25)). We also performed SBA-15-PAN@Ru (III) material using $NaBH_4$ at room temperature in the molar ratio of 1:1.7 (Ru^{+3}:BH_4^-) as per the reported literature [42]. Unfortunately, we obtained the Ru NPs in CATALYST 1A is quite a bigger size ((27.8 nm (±0.25)) due to incomplete reduction.

The above-mentioned variations in the size of the Ru NPs in the different catalysts can be explained based on the stabilizing ability of different types of amines in amine-functionalized SBA-15 material. Just like many other organic ligands and surfactants, the amine group in amine-functionalized SBA-15 was used as capping agents to synthesize ultrafine Ru nanoparticles. The Ru complex or Ru NPs in catalyst 1–3 are expected to have different degrees of interaction with the different amine ligand functionalized SBA-15 materials and therefore end up with different sizes. More

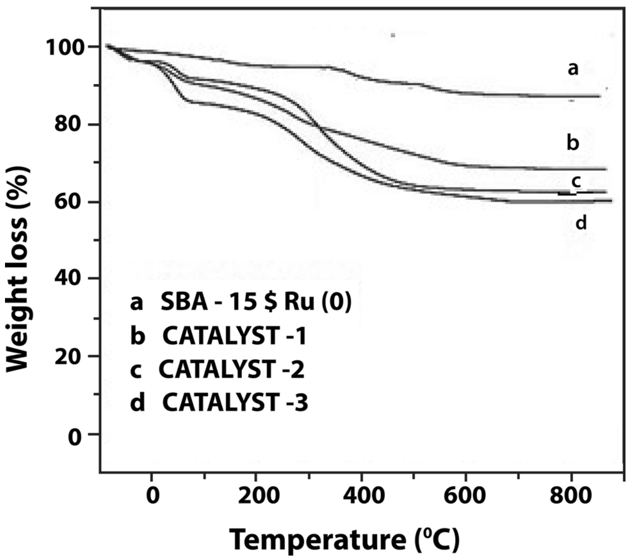

Fig. 5 TGA data for Ru doped amine functionalized SBA-15

specifically, tertiary amine ligands are weaker than primary and second to Ru complexions due to their poor solvation, hence they formed less thermodynamically stable Ru ion complex. Ru complexions or Ru NPs showed less stability within the pores of SBA-15 functionalized with more *N*-methylated amine ligands concerning less *N*-methylated or unmethylated counterparts. In other words, less interaction was recorded between the tertiary amine group with Ru NPs than a primary amine with Ru NPS. As a result of the above discussion, catalyst 3 gave bigger NPs.

The potential electronic interaction between the amine group and Ru NPs was elucidated using X-ray photoelectron spectroscopy (XPS) and all peaks related to Ru were carefully analyzed and showed in Fig. 7. Due to the presence of organoamine functional groups in the catalysts 1, 2, and 3 the peaks for the Ru 3d region showed two intense narrow peaks at binding energies of 280.4 and 284.3 eV for Ru 3d$_{5/2}$ and 3d$_{3/2}$, respectively (Fig. 7). These peaks can be assigned to metallic Ru as per the literature [43–45], which indicates that the composition of the NPs is mainly Ru (0) NPs. No noticeable change among the peak of Ru 3d in the

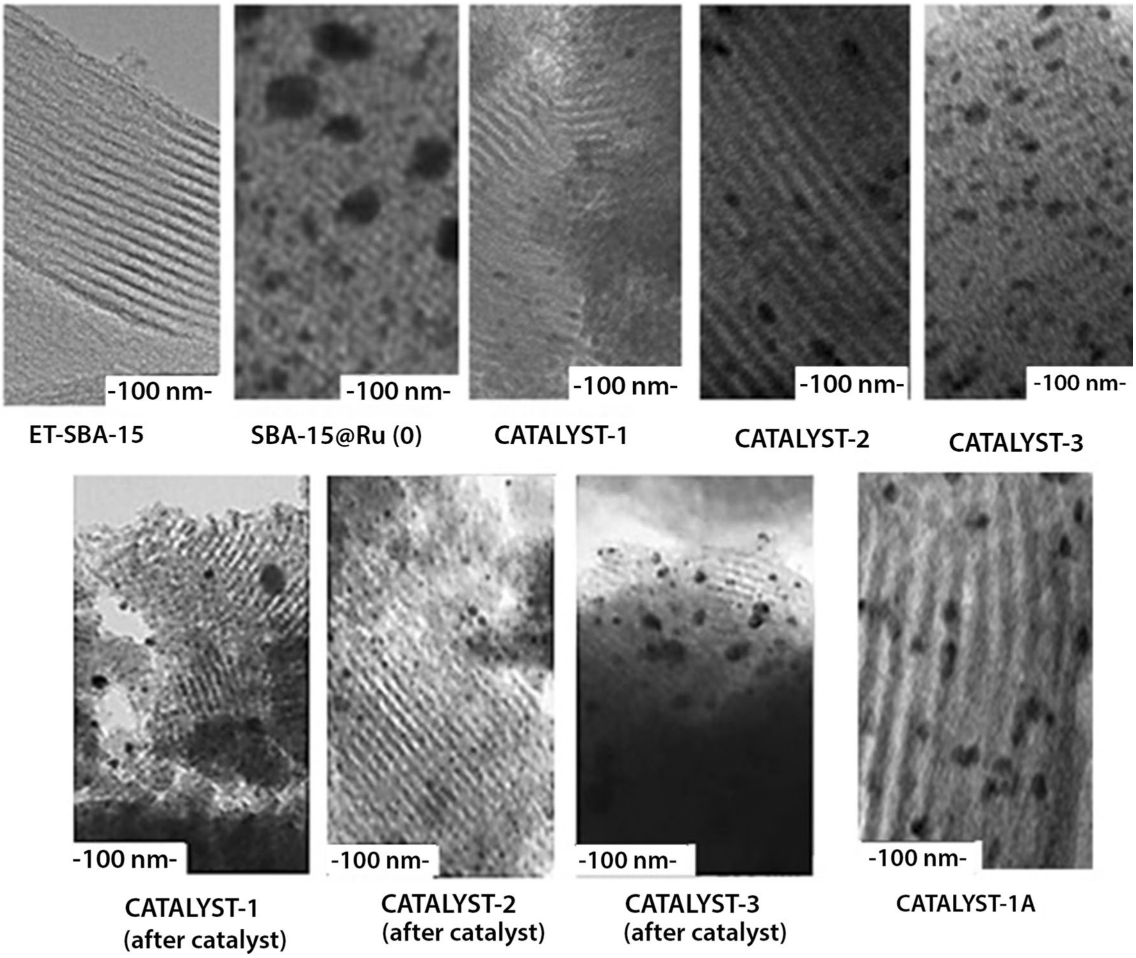

Fig. 6 TEM data of all the developed materials

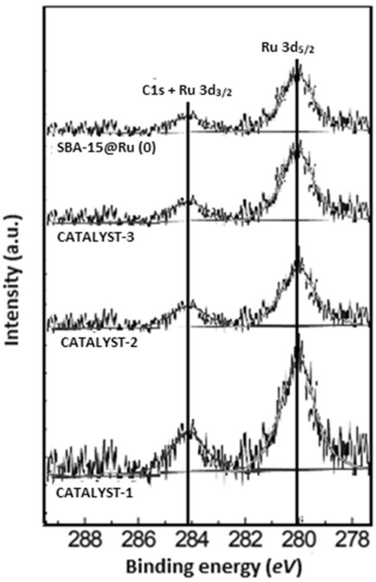

Fig. 7 XPs data of Ru doped amine functionalized SBA-15 materials

CATALYST-1, 2, and 3 were recorded while varying the nature of methyl substituents.

We also performed, the total hydrogenation chemisorption and the reversible hydrogen chemisorption at 25° C to identify the physical properties of all the developed CATALYST-1, 2 and 3. It was recorded that the total and the reversible H_2 adsorption isotherms became parallel above a pressure of 500 torr indicating the presence of equilibrium in adsorption above this pressure. The difference between the two isotherms at 740 torr is taken as a measure of irreversible H2 uptake [46–48]. The reversible and irreversible H_2 uptake and their ratios (H_r/H_{irr}) for the catalyst of different metals lodgings are presented in Table 3.

Table 3, confirmed a direct correlation between Ru metal loading and hydrogen uptake. The irreversible hydrogen uptake which corresponds to a stoichiometry of H_{irr}/Ru (0) = 1:1 increases with Ru loading and found maximum in the case of CATALYST-1.

The hydrogen chemisorption is also studied with CATALYST-1 at a different temperature from 25 °C to 300 °C (Fig. 8). The hydrogen uptake taken from the isotherm at 740 torr pressure is plotted against the temperature of adsorption in Fig. 9. It is seen that hydrogen uptake increases with temperature rise and passes through a maximum at 125 °C. The increase in H_2 uptake with temperature rise is mainly due to multiple bond adsorption or reversible H_2 adsorption on ruthenium sites science it is well established that strong and irreversible H_2 uptake corresponds to 1:1 stoichiometry of H_{irr}/Ru (0) does not change with temperature. The capacity of ruthenium atoms to form multiple bonds with hydrogen atoms on the catalyst surface is enhanced by raising the temperature of adsorption. The hydrogen chemisorption isotherm of CATALYST-1 is presented in Fig. 9. In which it is shown that the total hydrogen uptake at 740 torr increases up to 125 °C above which decreases drastically. Thus, the results of the present studies suggest that the reversible H_2 chemisorption plays an important role in the hydrogenation reaction on group VIII metals [46, 47, 47, 48].

3.3.1 Catalytic Activities of the Materials CO_2 Hydrogenation Reaction and Effect of Their Physicochemical Properties

The CO_2 hydrogenation reaction was carried out by placing the series of SBA-15-PAN@Ru (0) (CATALYST-1), SBA-15-SAN@Ru (0) (CATALYST-2), and SBA-15-TAN@Ru (0) (CATALYST-3) as per the given reaction conditions in

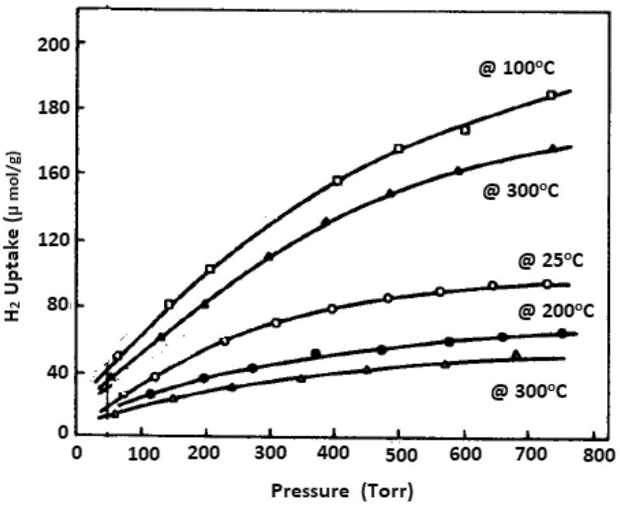

Fig. 8 H_2 chemisorption isotherm at different temperature

Table 3 Hydrogen chemisorption study

Material	BET^a surface area (m^2/g)	Ru (0)^b (mmol/g_{cat})	Reversible H_2 uptake (H_r) μ mol/g	Irreversible H_2 uptake (H_{irr}) μ mol/g	H_r/H_{irr}
CATALYST -1	185	0.43	85.0	25.2	3.37
CATALYST -2	197	0.15	62.7	10.2	6.14
CATALYST -3	243	0.16	63.5	7.8	8.14

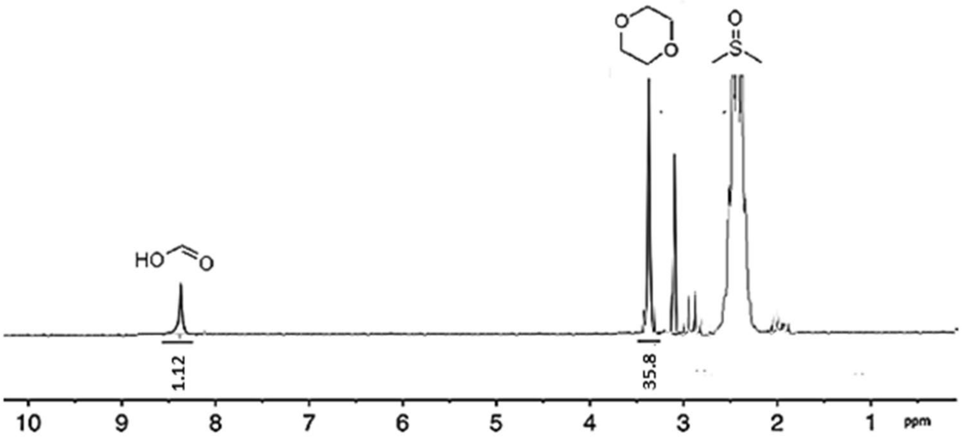

Fig. 9 ^{1}HNMR analysis of Reaction mass and formic acid calculation

Table 4. Among all the three catalysts, catalyst 1 gave higher catalyst activity and synthesized the formic acid in good quantity. After completion, the reaction and catalyst were isolated from the reaction mass followed by the centrifugation method, then a small quantity of reaction mass was used for titration and ^{1}H NMR analysis to quantify the amount of formic acid in the reaction mass. It is worth notify that the result obtained by the titration method and ^{1}HNMR (Fig. 9), were found in good agreement with each other. The activity of all three catalysts was measured in terms of formic acid quantity, TON, and TOF value, and all the results were summarized in Table 4. The catalytic performance of all three catalysts can be explained based on the physicochemical properties of the catalysts. In some of the recent reports, amine-functionalized mesoporous silica-supported metals

Table 4 Application of CATALYST 1, 2 and 3 for CO_2 hydrogenation reaction

S.No	Catalytic system (CATALYST 0.01 g + 5 ml Water)	*P* (H_2) (*P* $_{total}$) (MPa)	T°C	t (h)	Formic acid (g)	TON (mol_{FA}/mol_{Ru})	TON (mol_{FA}/ mol_{Ru} x h^{-1})
1	CATALYST-1	20 (40)	80	8	0.94	10,356.5	1294.6
2	CATALYST-2	20 (40)	80	8	0.88	885.2	110.7
3	CATALYST-3	20 (40)	80	8	0.67	5204.1	650.5
4	CATALYST-1 + 0.2 mL Et_3N + 5 mL Water	20 (40)	80	8	0.91	5090.2	636.3
5	CATALYST-1 + 0.2 g NaOH + 5 mL Water	20 (40)	80	8	0.36	2013.7	251.7
6	CATALYST 1 + 5 mL DMSO	20 (40)	80	8	0.51	2909.7	363.7
7	CATALYST-1 + 2 mL water	20 (40)	80	8	0.17	950.9	118.9
8	CATALYST-1 + 10 mL water	20 (40)	80	8	0.91	5035.3	629.4
9	CATALYST-1 (0.1 g)	20 (40)	80	8	0.90	5030.4	628.8
10	CATALYST-1 (0.005 g)	20 (40)	80	8	0.12	1342.5	167.8
11	CATALYST-1	10 (20)	80	8	0.30	1678.1	209.8
12	CATALYST-1	30 (60)	80	8	0.89	4978.3	622.3
13	CATALYST-1	20 (40)	100	8	0.82	4586.8	573.4
14	CATALYST-1	20 (40)	50	8	0.23	1390.4	173.8
15	CATALYST-1	20 (40)	80	4	0.28	1566.2	391.6
16	CATALYST-1	20 (40)	80	10	0.85	4754.6	475.5
17	CATALYST-1 + PPh_3 (0.2 g)	20 (40)	80	8	0.82	4586.8	573.4
18	SBA-15@Ru	20 (40)	80	8	0.41	1062.5	132.8
19	$RuCl_3.3H_2O$	20 (40)	80	8	0.12	17.8	2.2
20	$[Ru\ (NH_3)_6\ Cl_3]$	20 (40)	80	8	0.32	1810.2	226.3
21	$[Ru\ (NH_2\ CH_3)_6\ Cl_3]$	20 (40)	80	8	0.22	1231.8	154.0
22	$[Ru\ (NH\ (CH_3)_2)_6\ Cl_3]$	20 (40)	80	8	0.19	987.1	123.4
23	CATALYST-1a	20 (40)	80	8	0.87	4730.4	591.3

were found highly active for CO_2 hydrogenation reaction [49, 50].

The high catalytic performance of catalysts 1, 2, and 3 was ascribed to the electron density transfer from the primary amine groups to the Ru NPs, and thus the electron-richness of the Ru centers in it. The same electron transfer progression from secondary and tertiary amine groups to Ru NPs and comparable peak positions for Ru 3d in XPS analysis were also recorded for the Ru NPs in catalyst 2 and 3. Hence the catalytic activity of CATALYST-2 and 3, can be justified as per the above argument. Though, moreover, we can correlate the catalytic performance of CATALYST-1, 2, and 3 in the CO_2 hydrogenation reaction. A drop in HCOOH quantity was recorded while increasing the Ru particle size from 4.5–32.7 nm.

The CO_2 hydrogenation reaction is reported as a thermodynamically unfavorable transformation [17, 23]. To shift the reaction towards the formic acid formation, high pressure (> 2 MPa) and additives as amine, ammonia, or an alkali were explored to promote the formation of adduct or complex which support the easy reduction of CO_2 to formic acid. We also used the organic and inorganic base to achieve the same, despite considering the presence of amine functionality in our catalysts. No positive change in the quantity of formic acid was recorded, this confirms the additional benefits of using amine-functionalized support in our catalytic system.

We also examined the effect of the solvent system in our catalytic system. Apart from water, we also tested the polar aprotic DMSO solvent system in place of water. The low formic acid quantity was noticed while replacing the water with DMSO. In our study, we found that water plays an important role to accelerate the rate of CO_2 reduction as it reacts with water as well as amine during the reaction and form the bicarbonate species, which may work as a true reaction substrate for the hydrogenation [27, 51, 52]. Although, the presence of water not only increases the quantity of formic acid but also increases the energy consumption to remove water from the reaction mass. Hence, it is important to use water in an optimized quantity. During the water optimization, 5 mL of water was found sufficient to get the maximum amount of formic acid.

It is well documented that the quantity of catalyst plays an important role to change the rate of any chemical reaction [17, 23]. The same observation was recorded while lowering or increasing the catalyst quantity the noticeable change in the amount of formic acid was recorded. A drop in formic acid quantity was found while increasing the catalyst quantity signifies the formation of Ru agglomerates during the reaction. While using the optimized catalyst quantity, the Ru NPs get dispersed effectively in reaction mass and provides better contact between reactants and catalyst active sites.

It is well documented that CO_2 hydrogenation is a pressure-dependent reaction, but while changing the pressure of reactants in comparison with the optimized condition, and a clear drop in formic acid quantity was recorded. Drop-in formic acid quantity at low pressure can be explained by the weak interaction between catalyst and reactants. An increase in reactant pressure also lowers the quantity of formic acid due to the decomposition of formic acid at high pressure. This observation was also supported by previously reported literature [51]. A very low quantity of formic acid was noticed while performing the reaction at 50 °C, this confirms the low activation of reactants at the above temperature. Similarly, a small drop in formic acid quantity was recorded at a high temperature which supports the decomposition of formic acid at 100 °C under pressure or reverses water gas shift reaction. The optimized reaction condition of CO_2 hydrogenation was also checked with PPh_3 (triphenylphosphine) as an additive, but no significant change in the quantity of formic acid was recorded. We also utilized [Ru $(NH_3)_6$ Cl_3], [Ru $(NH_2$ $CH_3)_6$ Cl_3] and [Ru $(NH(CH_3)_2)_6Cl_3$] materials to catalyze the CO_2 reduction reaction but we obtained formic acid in low quantity (Table 4, entry 20–22). This confirms the importance of support in the catalytic system which also worked as a co-catalyst.

In the catalytic CO_2 hydrogenation reaction, we presented the *in-situ* Diffuse Reflectance Infrared with Fourier Transform Spectroscopy (DRIFT) analysis to explore the creation of surface species in the catalytic processes and to find the reaction mechanism. In this analysis, DRIFT spectra were scrutinized at increasing reaction temperatures, in the existence of the reactant mixture/products. Figure 10a, revealed the spectrum of ET-SBA-15 after the CO_2 adsorption (Table 5). The band at 1715 cm^{-1} could be allocated to the ν_S modes of bridge carbonate [28, 53–56]. While, the bands at 1573 and 1308 cm^{-1} are ascribed, respectively, to the ν_{as} (CO_3) and ν_S (CO_3) modes of bidentate carbonate [57, 58]. The band at 1555 cm^{-1} resembles ν_{CO} modes of bicarbonate species and the band at 1662 cm^{-1} to the ν_{CO} mode of carboxylate species [28, 54, 57, 58]. The 1628 cm^{-1} band is appointed to the δ_{OH} mode of physisorbed water on ET-SBA-15. This shows the various interface configurations of CO_2 molecules with ET-SBA-15.

Figure 10b, exposes the interaction spectra between ET-SBA-15 and HCOOH. The bands were specified based on IR surveys registered for SBA-15. In the spectrum ET-SBA-15, the bands of 2945 and 1735 cm^{-1} could be named to the ν_{CH} and ν_{CO} modes of molecularity adsorbed HCOOH [59–61]. In the arena of Fig. 11, the noticed bands at 3715 and 3648 $cm^{-1}$are allocated to ν_{OH} modes of isolated OH groups on ET-SBA-15. The strength of these bands declines with HCOOH adsorption, coupled with an expansion of the wide-ranging 3000–3400 cm^{-1} band of ν_{OH} modes of hydrogen bonding. This indicates that the insular OH groups on ET-SBA-15 contributed to the molecular adsorption of HCOOH via hydrogen bonding. New bands emerged at

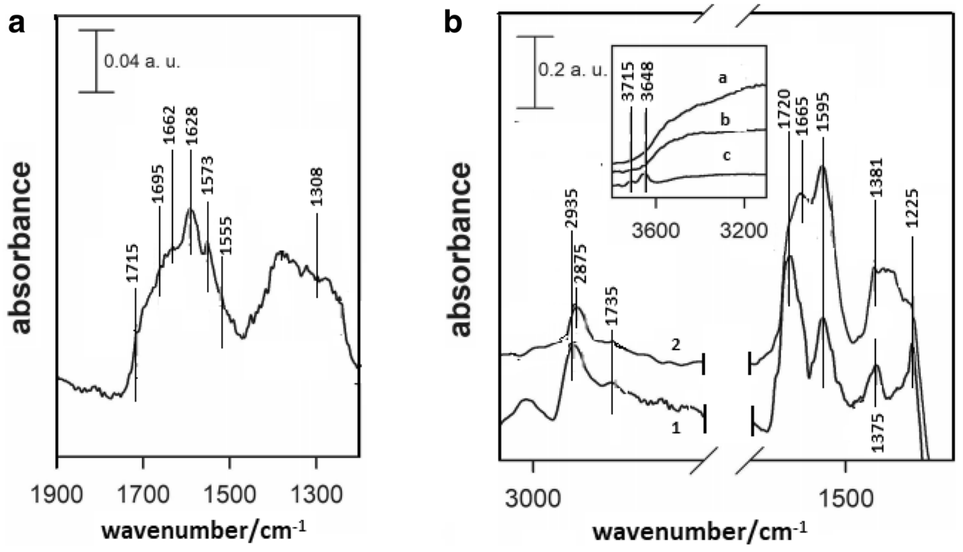

Fig. 10 **a** DRIFT analysis after CO_2 adsorption on CATALYST-1, **b** DRIFT analysis after CO2 adsorption on ET-SBA-15 (1) and CATALYST-1 (2) Inset spectra of ν_{OH} a. CATALYST-1 before HCOOH adsorption, b. CATALYST-1 after HCOOH adsorption and ET_SBA-15 after HCOOH adsorption

2875, 1595, and 1375 cm^{-1} credited to the ν_{CH}, ν_{asOCO}, and ν_{sOCO} modes of adsorbed $HCOO^-$ respectively [55, 57–62]. These findings suggest that HCOOH adsorbs in both molecular and dissociative forms on the ET-SBA-15 surface. In the CATALYST-1 spectrum, the aforementioned HCOOH adsorption bands on ET-SBA-15 are marginally dislocated. Bands of molecularly adsorbed HCOOH have redshift to 2935 cm^{-1} showed, assigned to the ν_{CO} mode of HCOOH adsorbed on the surface. These trapped band shifts could be a result of changes in the degree of surface hydration or sample pre-treatment. In this analysis, the CATALYST-1 were pre-reduced in H_2 at 45 °C while ET-SBA-15 was analyzed as prepared. Despite the dislocation, the band assignments are consistent with the development of surface species on the support site and not on the Ru site. The band assignments are summaries in Table 4 and the related species composition is displayed in Fig. 12.

The plausible mechanism of CO_2 hydrogenation to formic acid can be proposed in the following steps a. catalyst activation, b. H_2 dissociation, c. CO_2 insertion, d. hydride attack, e. formic acid desorption, and f. catalyst regeneration step (Scheme 2). Nanocrystalline Ru anchored in the cage-like structure of ET-SBA-15 can easily absorb the H_2 molecule on their active surface sites. These H_2 molecules were further dissociated and formed the highly reactive complex molecule with CO_2 gas. As per the reaction at the catalysts surface, followed by hydride attack on CO_2 molecule formic acid adduct formation takes place. The formic acid adduct molecule further gets desorbed from the catalyst surface via the catalyst regeneration step.

Table 5 Capture frequencies and band assignments after adsorption of CO_2 and HCOOH to the reduced CATALYS-1

Probe molecule	Captured frequencies (cm^{-1})	Assignment
CO_2	1715	ν_{CO} bridged carbonate
	1662	ν_{CO} carboxylate
	1573	ν_{asCO} bidentate carbonate
	1555	ν_{CO} bicarbonate
	1308	ν_{sCO} bidentate carbonate
HCOOH	2945–2935	ν_{CH} $HCOOH_{abs}$[a]
	2875	ν_{CH} $HCOO_{abs}$
	1735–1720	ν_{CO} $HCOOH_{abs}$
	1665	ν_{CH} $HCOOH_{sabs}$[b]
	1595	ν_{asoco} $HCOOH_{abs}$
	1375–1381	ν_{ssoco} $HCOOH_{abs}$

[a] Adsorbed

[b] Strongly adsorbed

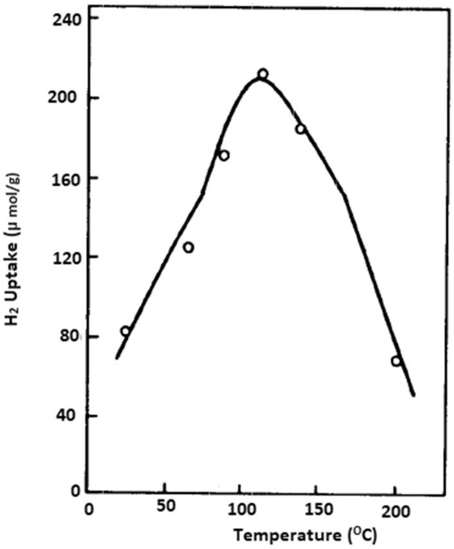

Fig. 11 H_2 chemisorption isotherm as a function of temperature

Fig. 12 Types of species identified in DRIFT study

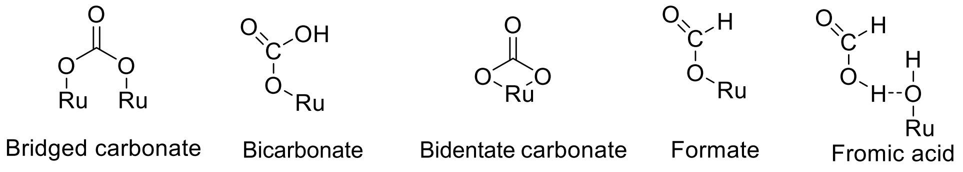

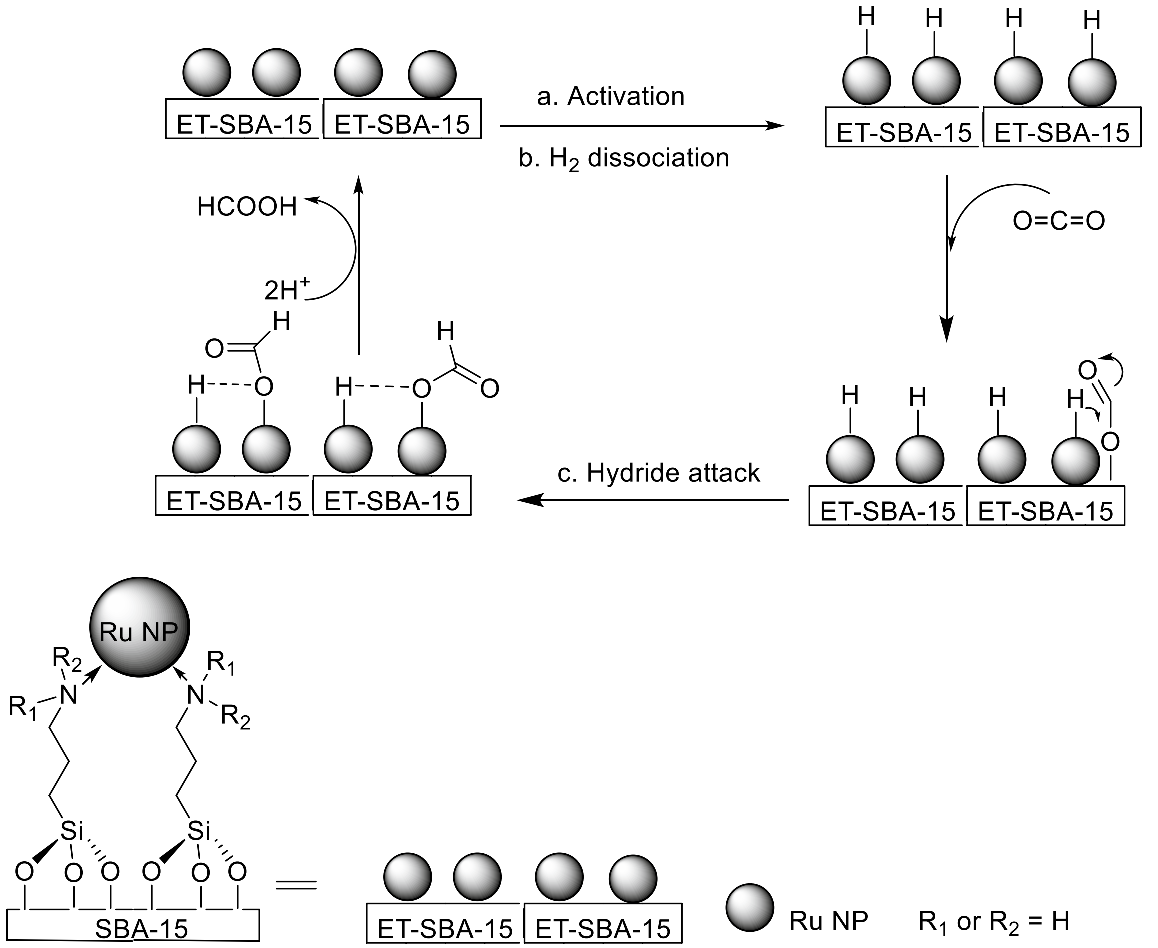

Scheme 2 Plausible mechanism of CATALYST-1 promoted CO_2 hydrogenation into the formic acid

3.4 Catalyst Recycling Study

Catalyst recyclability studies were conducted for all the catalysts to determine their stability and reusability under high-pressure reaction conditions. In the case of catalyst 1, we obtained effective recyclability up to 5 times in terms of formic acid quantity as well as TON and TOF values. While the other two catalysts were not found active after the 3rd run and we obtained a very low quantity of formic acid after recycling the CATALYST-2 and CATALYST-3 in the 4th recycling run (Fig. 10). We performed the TEM and ICP-OES analysis to understand better the physiochemical properties of all three catalysts during their recycling study. This study showed that the growth in Ru particle size as agglomeration was recorded after the 5th run in CATALYST-1 (25.8 nm (± 0.25)) and CATALYST-2 (39.9 nm (± 0.25)) and CATALYST-3 (45.9 nm (± 0.25)) gave the same result after their 3rd recycling run (Fig. 13). Also, a sign of Ru metal leaching was noticed maximum in the case of catalyst 2 and 3 in compression with catalyst 1. The above observations were found in good agreement with the application of amine group interaction with Ru metal. While achieving the satisfactory interaction of the amine group with Ru metal in CATALYST-1 lowered the process of agglomeration and metal leaching with respect to CATALYST- 2 and 3.

Fig. 13 Catalysts recycling experiment result

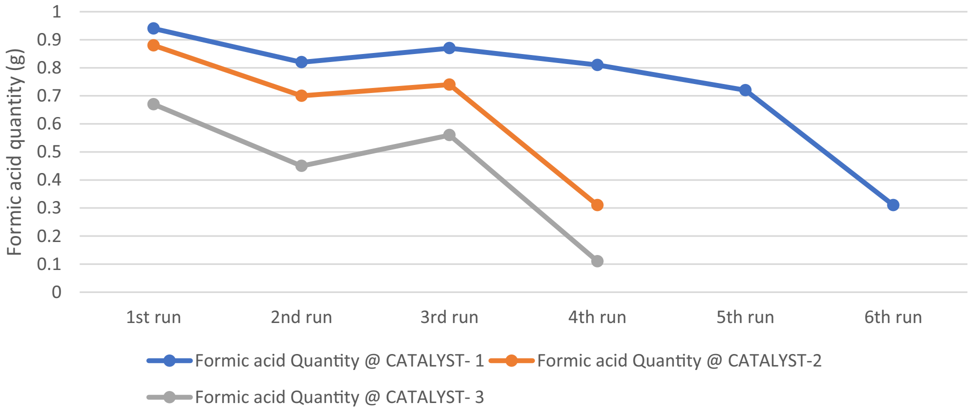

4 Conclusion

In summary, we have successfully synthesized a series of Ru metal immobilized-amine functionalized SBA-15 with different amine groups (SBA-15-PAN@Ru (0) (CATALYST-1), SBA-15-SAN@Ru (0) (CATALYST-2), and SBA-15-TAN@Ru (0) (CATALYST-3)). The structure, composition, and physicochemical properties of all the developed materials were analyzed by using different analytical techniques. All the analytical results were found in good agreement with each other. As per the analytical data of all the developed materials we clearly explained the relationship between amine groups and Ru NPs. The catalytic performance of all the materials was found in good agreement with their physiochemical properties like the amount of Ru NPs, surface area/pore size/pore volume of the catalysts. DRIFTS analysis verified the formation of various surface species bonded to the support such as carbonate and formate, while ruthenium carbonyl hydride species were found connected with Ru NPs. Considering DRIFTS analysis, we proposed the plausible mechanism of CO_2 hydrogenation into the formic acid with following steps a. catalyst activation, b. H_2 dissociation, c. CO_2 insertion, d. hydride attack, e. formic acid desorption, and f. catalyst regeneration step. This correlation of catalytic structure with their catalytic performance gave valuable guidelines to design other efficient catalysts for different types of tedious organic transformations.

Declarations

Conflict of interest The authors declare no conflict of interest, financial or otherwise.

References

1. Styring P, Quadrelli EA, Armstrong K (2014) Carbon dioxide utilisation: closing the carbon cycle: First Edition. Elsevier Inc.
2. Leung DYC, Caramanna G, Maroto-Valer MM (2014) An overview of current status of carbon dioxide capture and storage technologies. Renew Sustain Energy Rev 39:426–443
3. Aresta M (1999) Perspectives in the use of carbon dioxide. Quim Nova 22:269–272
4. F. Arajo O de Q, de Medeiros JL, Maria R (2014) CO2 utilization: a process systems engineering vision. In: CO2 sequestration and valorization. InTech
5. Liu Q, Wu L, Jackstell R, Beller M (2015) Using carbon dioxide as a building block in organic synthesis. Nat Commun 6:1–15
6. Artz J, Müller TE, Thenert K et al (2018) Sustainable conversion of carbon dioxide: an integrated review of catalysis and life cycle assessment. Chem Rev 118:434–504
7. Sakakura T, Choi JC, Yasuda H (2007) Transformation of carbon dioxide. Chem Rev 107:2365–2387
8. Hietala J, Vuori A, Johnsson P et al (2016) Formic Acid. Ullmann's Encyclopedia of Industrial Chemistry. Wiley-VCH Verlag GmbH and Co. KGaA, Weinheim, Germany, pp 1–22
9. Mellmann D, Sponholz P, Junge H, Beller M (2016) Formic acid as a hydrogen storage material-development of homogeneous catalysts for selective hydrogen release. Chem Soc Rev 45:3954–3988
10. Singh AK, Singh S, Kumar A (2016) Hydrogen energy future with formic acid: a renewable chemical hydrogen storage system. Catal Sci Technol 6:12–40
11. Centi G, Quadrelli EA, Perathoner S (2013) Catalysis for CO2 conversion: a key technology for rapid introduction of renewable energy in the value chain of chemical industries. Energy Environ Sci 6:1711–1731
12. Pérez-Fortes M, Schöneberger JC, Boulamanti A et al (2016) Formic acid synthesis using CO2 as raw material: techno-economic and environmental evaluation and market potential. Int J Hydrogen Energy 41:16444–16462. https://doi.org/10.1016/j.ijhydene.2016.05.199
13. Jo DY, Ham HC, Lee KY (2020) Facet-dependent electrocatalysis in the HCOOH synthesis from CO2 reduction on Cu catalyst: a density functional theory study. Appl Surf Sci. https://doi.org/10.1016/j.apsusc.2020.146857

14. Zhang Y, Zhang T, Das S (2020) Catalytic transformation of CO2 into C1 chemicals using hydrosilanes as a reducing agent. Green Chem 22:1800–1820
15. Leitner W (1995) Carbon dioxide as a raw material: the synthesis of formic acid and its derivatives from CO2. Angew Chemie Int Ed English 34:2207–2221
16. Reymond H, Corral-Pérez JJ, Urakawa A, Rudolf Von Rohr P (2018) Towards a continuous formic acid synthesis: a two-step carbon dioxide hydrogenation in flow. React Chem Eng 3:912–919. https://doi.org/10.1039/c8re00142a
17. Jessop PG, Ikariya T, Noyori R (1995) Homogeneous hydrogenation of carbon dioxide. Chem Rev 95:259–272. https://doi.org/10.1021/cr00034a001
18. Wang W-H, Feng X, Bao M (2018) Transformation of carbon dioxide to formic acid and methanol. Springer Singapore, Singapore
19. Wang W-H, Hime Y (2012) Recent advances in transition metal-catalysed homogeneous hydrogenation of carbon dioxide in aqueous media. In: Hydrogenation. InTech
20. Jessop PG, Ikariya T, Noyori R (1994) Homogeneous catalytic hydrogenation of supercritical carbon dioxide. Nature 368:231–233. https://doi.org/10.1038/368231a0
21. Wang W-H, Feng X, Bao M (2018) Transformation of CO2 to formic acid or formate with homogeneous catalysts. Springer, Singapore, pp 7–42
22. Jessop PG, Joó F, Tai CC (2004) Recent advances in the homogeneous hydrogenation of carbon dioxide. Coord Chem Rev 248:2425–2442
23. Ross JRH (2012) Heterogeneous catalysis – chemistry in two dimensions. In: Heterogeneous catalysis. Elsevier, pp 1–15
24. Gunasekar GH, Park K, Jung KD, Yoon S (2016) Recent developments in the catalytic hydrogenation of CO2 to formic acid/formate using heterogeneous catalysts. Inorg Chem Front 3:882–895
25. Bulushev DA, Ross JRH (2018) Heterogeneous catalysts for hydrogenation of CO2 and bicarbonates to formic acid and formates. Catal Rev Sci Eng 60:566–593. https://doi.org/10.1080/01614940.2018.1476806
26. Upadhyay PR, Srivastava V (2017) Ionic liquid mediated in situ synthesis of Ru nanoparticles for CO2 hydrogenation reaction. Catal Lett 147:1051–1060. https://doi.org/10.1007/s10562-017-1995-7
27. Gautam P, Upadhyay PR, Srivastava V (2019) Selective hydrogenation of CO2 to formic acid over alumina-supported Ru nanoparticles with multifunctional ionic liquid. Catal Lett 149:1464–1475. https://doi.org/10.1007/s10562-019-02773-z
28. Liu Q, Yang X, Li L et al (2017) Direct catalytic hydrogenation of CO2 to formate over a Schiff-base-mediated gold nanocatalyst. Nat Commun 8:1–8. https://doi.org/10.1038/s41467-017-01673-3
29. Masuda S, Mori K, Kuwahara Y et al (2020) Additive-free aqueous phase synthesis of formic acid by direct CO2 hydrogenation over a PdAg catalyst on a hydrophilic N-doped polymer-silica composite support with high CO2 affinity. ACS Appl Energy Mater 3:5847–5855. https://doi.org/10.1021/acsaem.0c00771
30. Wang W, Wang S, Ma X, Gong J (2011) Recent advances in catalytic hydrogenation of carbon dioxide. Chem Soc Rev 40:3703–3727. https://doi.org/10.1039/c1cs15008a
31. Xi J, Wang Q, Duan X et al (2020) Continuous flow reduction of organic dyes over Pd-Fe alloy based fibrous catalyst in a fixed-bed system. Chem Eng Sci 231:116303. https://doi.org/10.1016/j.ces.2020.116303
32. Martín-Jimeno FJ, Suárez-García F, Paredes JI et al (2021) Nickel nanoparticle/carbon catalysts derived from a novel aqueous-synthesized metal-organic framework for nitroarene reduction. J Alloys Compd 853:157348. https://doi.org/10.1016/j.jallcom.2020.157348
33. Liu J, Hao J, Hu C et al (2018) Palladium nanoparticles anchored on amine-functionalized silica nanotubes as a highly effective catalyst. J Phys Chem C 122:2696–2703. https://doi.org/10.1021/acs.jpcc.7b10237
34. Srivastava V (2016) Active heterogeneous Ru nanocatalysts for CO2 hydrogenation reaction. Catal Lett 146:2630–2640. https://doi.org/10.1007/s10562-016-1882-7
35. Srivastava V (2014) Ru-exchanged MMT clay with functionalized ionic liquid for selective hydrogenation of CO2 to formic acid. Catal Lett 144:2221–2226. https://doi.org/10.1007/s10562-014-1392-4
36. Fan J, Gao Y (2006) Nanoparticle-supported catalysts and catalytic reactions–a mini-review. J Exp Nanosci 1:457–475. https://doi.org/10.1080/17458080601067708
37. Kokunešoski M, Gulicovski J, Matović B et al (2010) Synthesis and surface characterization of ordered mesoporous silica SBA-15. Mater Chem Phys 124:1248–1252. https://doi.org/10.1016/j.matchemphys.2010.08.066
38. Allen AD, Senoff CV (1967) Preparation and infrared spectra of some ammine complexes of ruthenium(II) and ruthenium(III). Can J Chem 45:1337–1341. https://doi.org/10.1139/v67-220
39. Zhao D, Feng J, Huo Q et al (1998) Triblock copolymer syntheses of mesoporous silica with periodic 50 to 300 angstrom pores. Science 80(279):548–552. https://doi.org/10.1126/science.279.5350.548
40. Gu D, Schüth F (2014) Synthesis of non-siliceous mesoporous oxides. Chem Soc Rev 43:313–344
41. Hsu YC, Hsu YT, Hsu HY, Yang CM (2007) Facile synthesis of mesoporous silica SBA-15 with additional intra-particle porosities. Chem Mater 19:1120–1126. https://doi.org/10.1021/cm062167i
42. Anantharaj S, Jayachandran M, Kundu S (2016) Unprotected and interconnected Ru0 nano-chain networks: advantages of unprotected surfaces in catalysis and electrocatalysis. Chem Sci 7:3188–3205. https://doi.org/10.1039/c5sc04714e
43. Qadir K, Kim SM, Seo H et al (2013) Deactivation of Ru catalysts under catalytic CO oxidation by formation of bulk Ru oxide probed with ambient pressure XPS. J Phys Chem C 117:13108–13113. https://doi.org/10.1021/jp402688a
44. Carbonio EA, Prieto MJ, De SA, Landers R (2014) From 1D to 3D Ru nanostructures on a pt stepped surface as model systems in electrocatalysis: UHV-STM and XPS study. J Phys Chem C 118:28679–28688. https://doi.org/10.1021/jp509574s
45. Qadir K, Joo SH, Mun BS et al (2012) Intrinsic relation between catalytic activity of CO oxidation on Ru nanoparticles and Ru oxides uncovered with ambient pressure XPS. Nano Lett 12:5761–5768. https://doi.org/10.1021/nl303072d
46. Durndell LJ, Zou G, Shangguan W et al (2019) Structure-reactivity relations in ruthenium catalysed furfural hydrogenation. ChemCatChem 11:3927–3932. https://doi.org/10.1002/cctc.201900481
47. Lin B, Guo Y, Liu R et al (2018) Preparation of a highly efficient carbon-supported ruthenium catalyst by carbon monoxide treatment. Ind Eng Chem Res 57:2819–2828. https://doi.org/10.1021/acs.iecr.7b05077
48. Bus E, Miller JT, Van Bokhoven JA (2005) Hydrogen chemisorption on Al2O3-supported gold catalysts. J Phys Chem B 109:14581–14587. https://doi.org/10.1021/jp051660z
49. Koh K, Jeon M, Yoon CW, Asefa T (2017) Formic acid dehydrogenation over Pd NPs supported on amine-functionalized SBA-15 catalysts: structure-activity relationships. J Mater Chem A 5:16150–16161. https://doi.org/10.1039/c7ta02040f
50. Hiyoshi N, Yogo K, Yashima T (2005) Adsorption of carbon dioxide on aminosilane-modified mesoporous silica. J Japan Pet Inst 48:29–36. https://doi.org/10.1627/jpi.48.29

51. Pandey PH, Pawar HS (2020) Cu dispersed TiO2 catalyst for direct hydrogenation of carbon dioxide into formic acid. J CO2 Util 41:101267. https://doi.org/10.1016/j.jcou.2020.101267
52. Gautam P, Srivastava V (2020) Active γ –alumina -supported Ru nanoparticles for CO2 hydrogenation reaction. Lett Org Chem 17:603–612. https://doi.org/10.2174/157017861766619110711 2429
53. Danon A, Stair PC, Weitz E (2011) FTIR study of CO2 adsorption on amine-grafted SBA-15: elucidation of adsorbed species. J Phys Chem C 115:11540–11549. https://doi.org/10.1021/jp200914v
54. Liu MH, Chen HA, Chen CS et al (2019) Tiny Ni particles dispersed in platelet SBA-15 materials induce high efficiency for CO2 methanation. Nanoscale 11:20741–20753. https://doi.org/10.1039/c9nr06135e
55. Upadhyay PR, Srivastava V (2016) Heterogeneous silica tethered ruthenium catalysts for carbon sequestration reaction. Catal Lett 146:1478–1486. https://doi.org/10.1007/s10562-016-1772-z
56. Raskó J, Solymosi F (1994) Infrared spectroscopic study of the photoinduced activation of CO2 on TiO2 and Rh/TiO2 catalysts. J Phys Chem 98:7147–7152. https://doi.org/10.1021/j100080a009
57. Liu M, Zhang Q, Shi Y et al (2020) AuPd bimetal immobilized on amine-functionalized SBA-15 for hydrogen generation from formic acid: the effect of the ratio of toluene to DMF. Can J Chem Eng 98:879–891. https://doi.org/10.1002/cjce.23678
58. Farajzadeh M, Alamgholiloo H, Nasibipour F et al (2020) Anchoring Pd-nanoparticles on dithiocarbamate-functionalized SBA-15 for hydrogen generation from formic acid. Sci Rep 10:18188. https://doi.org/10.1038/s41598-020-75369-y
59. Mielby J, Kunov-Kruse AJ, Kegnæs S (2017) Decomposition of formic acid over silica encapsulated and amine functionalised gold nanoparticles. J Catal 345:149–156. https://doi.org/10.1016/j.jcat.2016.11.020
60. Luo Y, Yang Q, Nie W et al (2020) Anchoring IrPdAu nanoparticles on NH2-SBA-15 for fast hydrogen production from formic acid at room temperature. ACS Appl Mater Interfaces 12:8082–8090. https://doi.org/10.1021/acsami.9b16981
61. Bhattacharyya K, Danon A, Vijayan BK et al (2013) Role of the surface lewis acid and base sites in the adsorption of CO2 on titania nanotubes and platinized titania nanotubes: an in situ FT-IR study. J Phys Chem C 117:12661–12678. https://doi.org/10.1021/jp402979m
62. Nie W, Luo Y, Yang Q et al (2020) An amine-functionalized mesoporous silica-supported pdir catalyst: boosting room-temperature hydrogen generation from formic acid. Inorg Chem Front 7:709–717. https://doi.org/10.1039/c9qi01375j